CdS@TiO2 and ZnS@TiO2 core–shell nanocomposites: Synthesis and optical properties

3 AUTHORS:

Sonalika Vaidya
University of Delhi
21 PUBLICATIONS **429** CITATIONS

SEE PROFILE

Amitava Patra
Indian Association for the Cultivation of Science
172 PUBLICATIONS **4,161** CITATIONS

SEE PROFILE

Ashok K. Ganguli
Indian Institute of Technology Delhi
313 PUBLICATIONS **2,950** CITATIONS

SEE PROFILE

# Shell Thickness Dependent Photocatalytic Properties of ZnO/CdS Core−Shell Nanorods

Sunita Khanchandani,[†] Simanta Kundu,[‡] Amitava Patra,[‡] and Ashok K. Ganguli*,[†]

[†]Department of Chemistry, Indian Institute of Technology, Hauz Khas, New Delhi 110016, India
[‡]Department of Materials Science, Indian Association for the Cultivation of Science, Kolkata, 700 032, India

Ⓢ *Supporting Information*

ABSTRACT: Core/shell nanorod arrays of ZnO/CdS have been synthesized with varying shell thickness and their shell thickness dependent photocatalytic properties have been investigated. Core/shell nanorod arrays of core diameter of 100 nm with variable shell thickness (10−30 nm) are synthesized by varying the concentration of the citric acid. XRD analysis reveals that tensile strain is obtained for ZnO nanorods and the compressive strain is obtained for core/shell nanorods. The UV−visible absorption spectra of the core/shell nanorod arrays show a red shift of the band edge of uncoated ZnO with shell growth. Steady-state photoluminescence (PL) spectra of the core/shell nanorod arrays show red shift of emission band with the increase in shell thickness. Decay kinetics indicate that the average lifetime ($\langle \tau \rangle$) of the core/shell nanorod arrays is larger than that of the uncoated ZnO nanorods due to charge separation. I−V studies show a 16-fold enhancement in current using the ZnO/CdS core/shell nanorod arrays having CdS shell thickness of 30 nm as compared to bare ZnO nanorods. The photocatalytic studies confirmed that the ZnO/CdS core/shell nanorod arrays exhibit improved degradation efficiency compared to bare ZnO and CdS under simulated solar radiation. The core/shell nanorods having shell (CdS) thickness of 30 nm displays the highest photocatalytic efficiency for the degradation of rhodamine B under simulated solar radiation, indicating efficient separation of electron−hole pairs. The mechanism of the photodegradation of RhB is given to elucidate the efficiency enhancement of ZnO/CdS photocatalysts. These results demonstrate that the ZnO/CdS core/shell nanorod arrays provide a facile and compatible frame for potential applications in nanorod-based solar cells and as efficient photocatalysts.
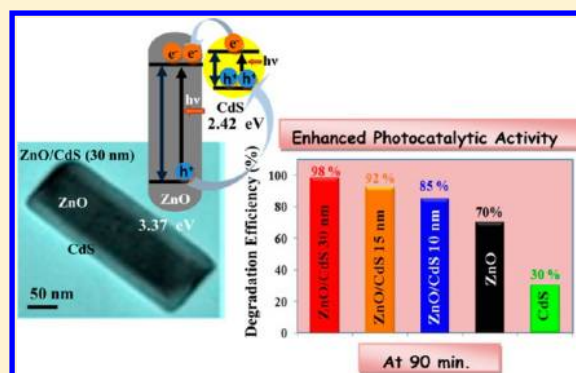
■ INTRODUCTION

Semiconductor nanostructures[1] have been of interest due to their wide ranging applications. Among various semiconductor nanomaterials, metal-oxides such as ZnO (bulk band gap of 3.37 eV) and TiO$_2$ (bulk band gap of 3.2 eV) have been studied intensively as photocatalysts because of their suitable band gap, high photocatalytic activity, and stability against photo-corrosion.[1−10] In particular, ZnO nanomaterials exhibit a few distinct advantages over TiO$_2$. The direct band gap of ZnO (3.37 eV), simple tailoring of structures, ease of crystallization, anisotropic growth, higher exciton binding energy of 60 meV (compared to 4 meV of TiO$_2$) and higher electron mobility (200 cm^2 V^{-1} s^{-1} compared to 30 cm^{2}V^{-1} s^{-1} for TiO$_2$) gives it an edge over TiO$_2$.[4−8] However, bare ZnO is known to have a wide band gap, which is disadvantageous for the absorption and use of the visible range of solar energy. To use visible light and the enhancement of photocatalytic efficiency of these metal-oxide semiconductors, it is necessary to couple them with a lattice matched photosensitizer.[11] Narrow/mid band gap semiconductor nanocrystals, dye molecules, and metal nano-particles are widely used as sensitizers on the surface of photocatalysts to capture additional visible light and con-sequently enhance the photocatalytic efficiency. Semiconduc-tors such as CdS,[12] CdSe,[13] PbS,[14] InP,[15] Ag$_2$S,[16] and Bi$_2$S$_3$,[17] which absorb light in the visible region, can serve as sensitizers, as they are able to transfer electrons to large band gap semiconductors. For an efficient electron transfer between the sensitizer and the photocatalyst, the energy level of the conduction band of the photocatalyst must be lower than that of the sensitizer. Thus, the electrons created in sensitizers are subsequently injected into the photocatalyst conduction band to perform a reduction reaction. The charge injection from narrow/mid band gap semiconductor into a wide band gap semiconductor can lead to efficient and longer charge separation by decreasing the recombination.[18] Among the most widely used inorganic semiconductor sensitizers, CdS (Bulk band gap 2.42 eV) is considered to be the most suitable visible sensitizer for ZnO; in particular, it has a high optical absorption coefficient and a similar lattice as of ZnO, which could facilitate a close interaction between the two semiconductors.[19] Another way to improve the photocatalytic efficiency is to create one-dimensional ZnO nanostructures that provide an ideal

geometrical structure for effective carrier transport and therefore reduces the charge recombination and increases the efficiency of ZnO photocatalyts.[20−23] The ability to form uniform CdS shell layers on one-dimensional nanostructures (ZnO nanorod arrays) with control of the shell thickness is a key step toward the realization of high-efficiency photocatalysts. Such core/shell nanorod structures of ZnO/CdS should form type-II band alignment, which facilitate the effective injection of photogenerated electrons from CdS into ZnO and reduces the rate of recombination between electron−hole pairs. In type-I core/shell heterostructures, both the electrons and the holes are confined in the core; in contrast, in type-II structures, the electrons and holes are separated between the core and the shell, giving rise to a significant increase in the exciton lifetime, which is advantageous for applications in both solar cells and photocatalysis.[45] There have been many reports on the fabrication of CdS nanoparticle/ZnO nanowire heterostructures that can efficiently separate and transfer electron−hole pairs in each semiconductor material, reduce their recombination, and improve photovoltaic efficiency.[24−28] However, there are few reports of CdS-ZnO composite nanorods to enhance the photocatalytic efficiency.[29] In addition, the optical, electrical, and photocatalytic properties of ZnO/CdS core/shell nanorod arrays with varying shell thickness has not been reported so far.

In this work, we report the surface-functionalized synthesis route for synthesizing the type-II ZnO/CdS core/shell nanorod arrays and the effect of the shell thickness on decay dynamics, optical, electrical, and photocatalytic properties of the ZnO/CdS core/shell nanorod arrays. It is found that these core/shell nanorod arrays show enhanced visible light absorption and photocatalytic activity for degrading rhodamine B (RhB) due to efficient charge separation and high transfer efficiency of photogenerated electrons. Finally, the possible mechanism of the visible light photocatalytic activity of ZnO/CdS core/shell nanorod arrays for degradation of RhB is studied in detail.

■ EXPERIMENTAL SECTION

Preparation of ZnO Nanorods. Zinc acetate dihydrate was used as the precursor for synthesizing ZnO nanorods.[30] A total of 0.5 g of the precursor was placed in an alumina crucible, covered by a lid, and then placed in a furnace. The crucible was heated to 300 °C and held for a period of 12 h, producing ZnO nanorods in powder form.

Preparation of CdS Nanoparticles. CdS nanoparticles were synthesized[31] using cadmium chloride and thiourea as precursors. In a typical procedure, 0.01 mol of cadmium chloride and 0.03 mol of thiourea were, separately, dissolved in 50 mL of ethylene glycol. Next, the cadmium solution and the thiourea solution were mixed together and loaded in a 100 mL Teflon autoclave. The reaction mixture was heated at 180 °C for 1 h and then air cooled at room temperature. The yellow product was separated by centrifugation and washed with absolute ethanol.

Preparation of ZnO/CdS Core/Shell Nanorod Arrays. Surface functionalization route[32] was used to prepare CdS-coated ZnO nanorods. First, 0.7 mmol of ZnO nanorods was dispersed in 50 mL of deionized water containing different amounts of citric acid (CA) under constant stirring. The solution was heated at 40 °C for 2 h and cooled to room temperature gradually. The aqueous solution of ZnO became fluffy, indicating that the ZnO nanorod surfaces were functionalized by the citrate ions. In the next step, a 25 mL

aqueous solution of 0.7 mmol of $CdCl_2$ was slowly added drop by drop to the ZnO solution under constant magnetic stirring for 2 h. Finally, 1.4 mmol of $Na_2S\cdot 9H_2O$ was dissolved in 25 mL of deionized water, slowly added dropwise to the system, and stirred for another 1 h at room temperature. This dropwise injection of precursors is very important to slow down the ion-exchange reaction between $[Zn^{2+}O^{2-}]$ ions and $[Cd^{2+}S^{2-}]$ ions through the surface of ZnO core because the normal CdS exchange process is so fast that the ZnO core cannot survive. The solution gradually turned yellow, indicating the formation of CdS layer over the ZnO nanorods. The sample synthesized using 0.095 mmol of CA was designated as ZnO/CdS1, 0.19 mmol of CA as ZnO/CdS2, and 0.38 mmol of CA as ZnO/CdS3. The different loading of CA for synthesizing ZnO/CdS core/shell nanorod arrays with varying shell thickness is summarized in Table S1. The products were separated by centrifugation and washed repeatedly with water and alcohol and then dried at 60 °C to obtain the fine powder.

■ CHARACTERIZATION

Powder X-ray diffraction studies (PXRD) were carried out on a Bruker D8 Advance diffractometer using Ni-filtered Cu Kα radiation. Normal scans were recorded with a step size of 0.02° and step time of 1s. Raw data was subjected to background correction and the Kα₂- lines were stripped off. Crystallite sizes (D, in Å) were estimated from the Scherrer's equation:

$$D = K\lambda/\beta \cos \theta \qquad (1)$$

where λ is the wavelength of Cu Kα radiation, β is the corrected half-width of the diffracted peak, θ is the angle, and K is equal to 0.9.

The lattice strain was calculated using the Williamson and Hall method:[47]

$$\beta \cos \theta/\lambda = 1/D + \eta \sin \theta/\lambda \qquad (2)$$

where β is the full width at half-maximum (fwhm), θ is the diffraction angle, λ is the X-ray wavelength, D is the crystallite size, and η is the effective strain. The strain is calculated from the slope, and the crystallite size (D) is calculated from the intercept of a plot of $\beta \cos \theta/\lambda$ against $\sin \theta/\lambda$.

The morphology of the samples was studied using a field emission scanning electron microscope (FESEM, JEOL, JSM-6700F). The nanostructures were observed using a transmission electron microscope (TEM JEOL 2010). For the TEM observations, the powders were dispersed in ethanol and ultrasonicated for 15 min. A few drops of this solution was taken on a carbon-coated copper grid. Compositional analysis was performed by energy dispersive X-ray spectroscopy (EDX) attached to a TEM. Optical absorption spectra were recorded on a UV-2401 PC Shimadzu spectrophotometer in the wavelength range of 325−650 nm by dispersing the samples in ethanol. Photoluminescence (PL) emission spectra were recorded by a Jobin Yvon-Spex Fluorolog spectrophotometer. Time-resolved PL studies were performed with a time correlated single-photon counting system of Horiba Jobin Yvon using 340 nm nano-LED as an excitation source.

I−V Measurements. The devices for the measurement of current−voltage (I−V) characteristic were prepared by the following procedure. A thin layer (100 nm) of Au was deposited by sputter coating (using an Eiko IB-2 ion coater) on a degreased glass substrate, which has a narrow wire rounded over it. After deposition, on removing the wire from the glass substrate, a narrow tunnel appeared. Then a small amount of a
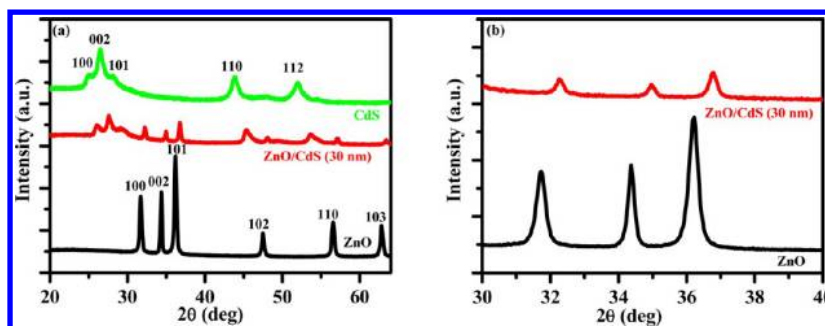
23654

dx.doi.org/10.1021/jp3083419 | J. Phys. Chem. C 2012, 116, 23653−23662

Figure 1. (a) XRD patterns of the uncoated ZnO nanorods, CdS nanoparticles, and ZnO/CdS core/shell nanorod arrays (ZnO/CdS3) and (b) XRD patterns of pure ZnO nanorods and ZnO/CdS3, indicating the shift in the peak position due to core/shell formation.

Table 1. Crystallite Size, Cell Parameters, and Lattice Strain of ZnO and ZnO/CdS Core/Shell Nanorod Arrays with Varying Shell Thickness

sample	shell thickness (nm)	crystallite size (Scherrer equation) (nm)	crystallite size (Williamson–Hall plot) (nm)	cell parameter (Å)	lattice strain (%)
ZnO		32.5	33.3	$a = 3.256(2)$ $c = 5.219(4)$	+0.33
ZnO/CdS1	10	28.8	29.5	$a = 3.252(2)$ $c = 5.216(2)$	−0.40
ZnO/CdS2	15	26.3	26.6	$a = 3.249(4)$ $c = 5.214(2)$	−0.51
ZnO/CdS3	30	11.4	11.80	$a = 3.244(2)$ $c = 5.209(7)$	−0.75

paste (in ethanol) of the prepared sample was placed in the narrow tunnel. The paste was allowed to dry naturally in air to form a thin layer. Thus, a two-probe device of Au–sample–Au was formed. The device was put into a shielded vacuum chamber, and an electrometer (Keithley 6517B) was connected between the two gold electrodes. The $I–V$ characteristics of the devices were recorded with the electrometer at room temperature.[32]

Photocatalytic Experiments. The photocatalytic properties of ZnO nanorods, CdS nanoparticles, and ZnO/CdS core/shell nanorod arrays with varying shell thickness were measured by the degradation of rhodamine B (RhB) in aqueous solution under simulated solar radiation. In a typical process, 20 mg of the sample was dispersed in 80 mL of 1.0×10^{-5} M RhB aqueous solution. The dye solution with the catalyst was stirred in the dark for 2 h until the equilibrium adsorption was attained. No significant decrease in the concentration of the dye was observed after 2 h for all the experiments. Experiments without simulated solar radiation in the presence of the catalyst, and experiments with simulated solar radiation in the absence of catalyst, showed no degradation of dye. The solution was then exposed to simulated solar radiation with a perfectly transparent glass plate to cover the top. The beaker was kept in an ice-cold water bath to ensure that the temperature was maintained and the degradation was only the result of photocatalytic activity. Samples were taken at regular intervals and centrifuged to remove the catalyst particles. The clear supernatant solution was analyzed in a UV–vis spectrophotometer (measured at 555 nm) to determine the concentration of RhB.[33] The degradation efficiency of the RhB can be defined as follows:

$$degradation(\%) = (1 - C/C_0) \times 100 \qquad (3)$$

where C_0 is the concentration of RhB at adsorption equilibrium and C is the residual concentration of RhB at different illumination intervals.

The photodegradation of RhB follows pseudo-first-order kinetics. Its kinetics can be expressed as

$$\ln(C_0/C) = kt \qquad (4)$$

where k (min^{-1}) is the degradation rate constant.

Analysis of Hydroxyl Radicals (OH•). Hydroxyl radicals (OH•) produced by the as-prepared photocatalysts under simulated solar radiation were measured by fluorescence method using terephthalic acid (TA) as probe molecule. In brief, 5 mg of ZnO/CdS sample was dispersed in 30 mL of a 5×10^{-4} M TA aqueous solution with a concentration of 2×10^{-3} M NaOH. Then, the resulting suspension was exposed to simulated solar light. At regular intervals, 1.2 mL of the suspension was collected and centrifuged to measure the maximum fluorescence emission intensity with an excitation wavelength of 315 nm.

■ RESULTS AND DISCUSSION

The reaction conditions were optimized for the synthesis of ZnO/CdS core/shell nanorod arrays by varying the cadmium and sulfur precursor concentration as well as by using different amounts of citric acid (CA). Finally, three core/shell products with different shell thicknesses were obtained by using different CA concentration. The crystalline phases of the products were identified by X-ray studies. Figure 1a shows the XRD patterns of the ZnO nanorods, CdS nanoparticles and ZnO/CdS core/shell structures having shell thickness of 30 nm (ZnO/CdS3). (XRD patterns of ZnO/CdS1 and ZnO/CdS2 are not shown here.) The XRD pattern of the uncoated ZnO nanorods shows a highly crystalline hexagonal phase (wurtzite structure) of ZnO (JCPDS card no. 36–1451). In the XRD pattern of core/shell ZnO/CdS additional peaks at 25.96° (100), 27.55° (002), 32.23° (101), 45.21° (110), and 53.62° (112) clearly indicate the existence of the hexagonal phase of the CdS shell (JCPDS card no. 41–1049) along with the hexagonal phase of ZnO. The formation of the CdS shell is further supported by XRD
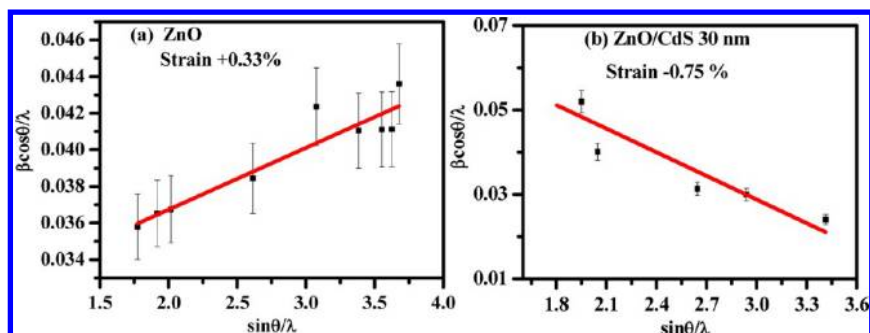
Figure 2. Williamson−Hall plot of $\beta \cos \theta / \lambda$ against $\sin \theta / \lambda$ for (a) pure ZnO nanorods and (b) ZnO/CdS3.
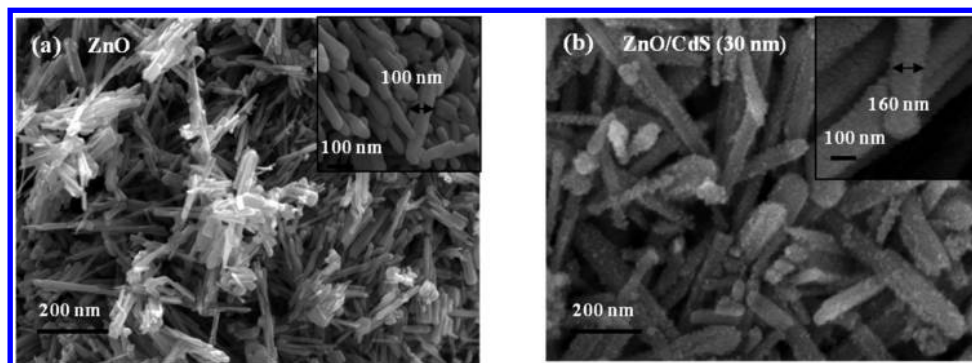

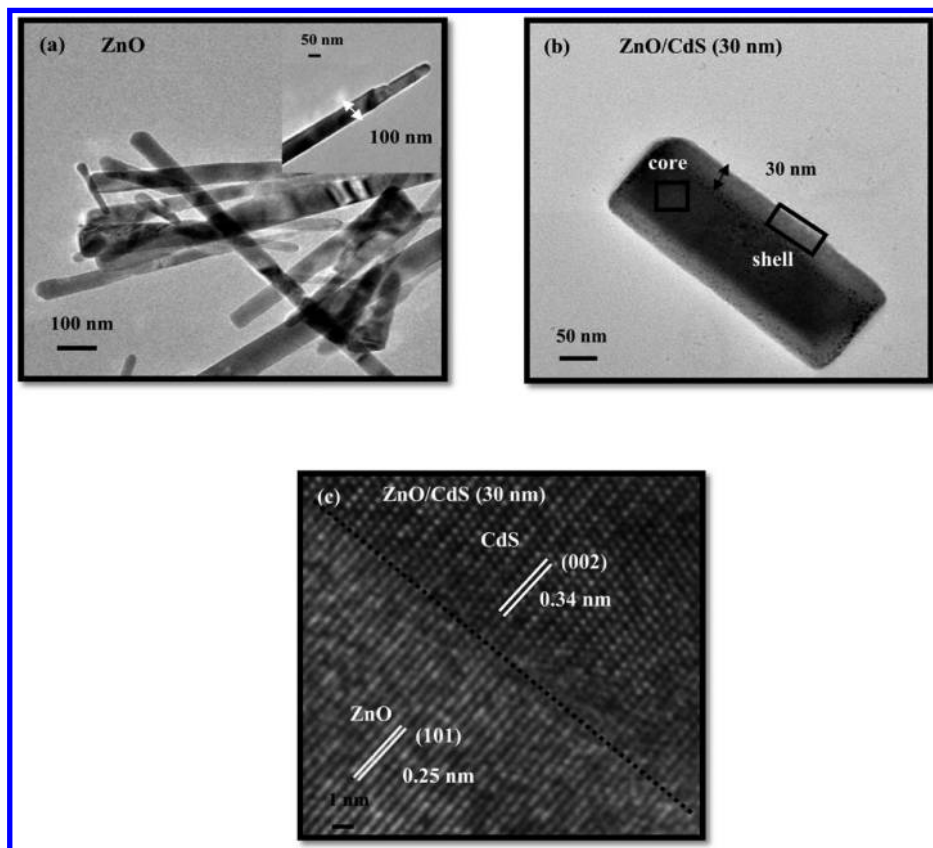**Figure 3.** FESEM images of (a) ZnO nanorods and (b) ZnO/CdS3.

Figure 4. TEM images of (a) ZnO nanorods, (b) ZnO/CdS3, and (c) HR-TEM of ZnO/CdS3.

analysis. The XRD pattern of ZnO nanorods (Figure 1a) consists of the characteristic hexagonal phase with reflections at 31.76, 34.36, 36.22, 47.47, 56.60, and 62.87°. A gradual shift of the diffraction maxima corresponding to ZnO toward larger angles at 32.23, 34.89, 36.81, 48.09, 57.13, and 63.40° with shell growth further confirms the formation of core/shell nanostruc-

Table 2. Best Fitted Parameters of Multiexponential Components Defined in Eqs 5−7

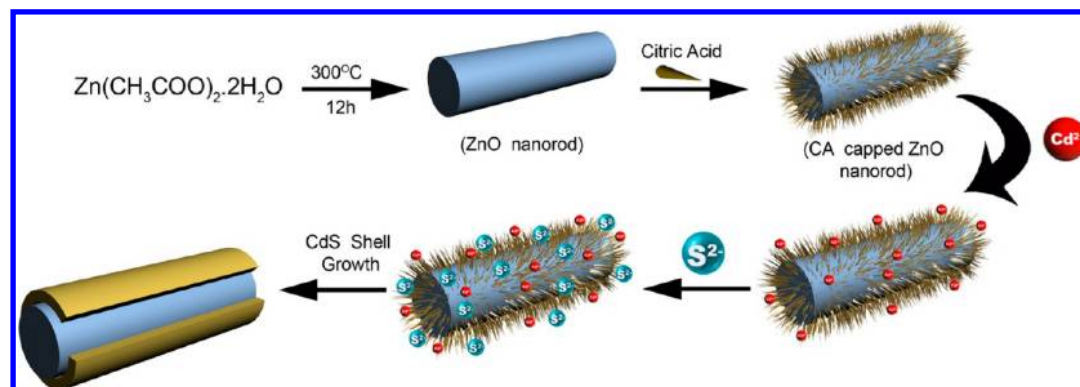| sample	shell thickness (nm)	τ_1 (ns; f_1)	τ_2 (ns; f_2)	τ_3 (ns; f_3)	$\langle\tau\rangle$ (ns)	goodness of fit parameter (χ^2)
ZnO		5.19 (0.0008)	0.061 (0.99)	219.5 (0.0006)	0.19	1.04
ZnO/CdS1	10	3.94 (0.0094)	0.110 (0.98)	211.0 (0.0051)	1.22	1.09
ZnO/CdS2	15	4.37 (0.0101)	0.129 (0.98)	211.1 (0.0057)	1.37	1.13
ZnO/CdS3	30	4.40 (0.0228)	0.147 (0.96)	213.5 (0.0157)	3.59	1.12

Figure 5. Schematic diagram showing the steps of formation of ZnO/CdS core/shell nanorod arrays by a surface-functionalization method.

tures.[47] This shift to higher angles in the core/shell structure (Figure 1b) is due to a smaller lattice constant for ZnO/CdS core/shell nanorod arrays compared with bare ZnO nanorods (Table 1). Wang et al.[34] observed the shift of the diffraction peaks to larger angles located between the cubic CdSe and CdS phase in CdSe/CdS core/shell nanocrystals. Similar changes in the diffraction pattern were also reported for other core/shell nanostructures.[35−37] Figure 2a shows a plot of $\beta\cos\theta/\lambda$ against $\sin\theta/\lambda$ for pure ZnO nanorods (using eq 2) and the slope value is +0.0033. The positive slope value indicates the tensile strain. The obtained crystallite size is 33.3 nm (from intercept), which is in good agreement with the calculated value from Scherrer equation (Table 1). Tensile strain is defined as the deformation along a line segment that increases in length when a load is applied along that line. Figure S1a represents a plot for ZnO/CdS core/shell nanorod arrays having a shell thickness of 10 nm and a negative slope (−0.0040) is obtained. It indicates the presence of compressive strain (−0.40%). The crystallite size is found to be 29.5 nm, which is well matched with the calculated value of 28.8 nm using Scherrer equation. As the shell is grown and its thickness increases, the diffraction peaks shift toward smaller d-spacing (larger 2θ). This means that the growth of the CdS shell is compressing the lattice planes in the ZnO core and that the compression increases as a function of shell thickness as is clear from Figures 2 and S1. Compressive strain is defined as the deformation along a line segment that decreases in length when a load is applied. It is interesting that the crystallite size of the core/shell samples is lower than that of the pure ZnO nanorods (Table 1). A strong dependence of crystallite size upon the induced strain by shell has been found. The results indicate that tensile strain exists in pure ZnO nanorods, whereas compressive strain is obtained after surface coating and strain is relaxed in larger crystallite size. The surface coating by CdS increases the compressive strain and, thus, leads to smaller crystallite size. Therefore, it suggests that the surface coating plays an important role in tuning the crystallite size and lattice strain of core/shell nanostructures. A similar kind of observation was observed for the Eu^{3+}-coated TiO$_2$ particles.[50]

The formation of core/shell nanostructures with CdS shell is also observed by FESEM images. Figure 3a shows the FESEM image of the uncoated ZnO nanorods with an average diameter of about 100 nm and a length of 500−600 nm with smooth surfaces. The inset of the Figure 3a shows the enlarged picture of the nanorods. After the CdS shell growth, the ZnO nanorod surfaces became rough (Figure 3b). The inset of Figure 3b shows the magnified image of the nanorod arrays from where the average diameter of the ZnO/CdS core/shell nanorods (ZnO/CdS3) was calculated and found to be 160 nm.

Shell growth of CdS on ZnO is further confirmed by the TEM and HRTEM images (Figure 4). The TEM image (Figure 4a) of uncoated ZnO nanorods shows average diameter of 100 nm with smooth surfaces and the inset is the enlarged image of a single ZnO nanorod. The apparent contrast in the TEM micrograph between the ZnO core and the CdS shell offers evidence for the formation of ZnO/CdS core/shell nanorod arrays, as shown in Figures S2a,b and 4b. The images show that the surface coating of the nanorods corresponding to ZnO/CdS3 is very uniform compared to that of the nanorods of ZnO/CdS1 and ZnO/CdS2. The thickness of the shell layers of samples ZnO/CdS1, ZnO/CdS2, and ZnO/CdS3 were calculated to be ∼10, 15, and 30 nm, respectively (Table 2). Thus, it may be concluded that the shell thickness increases with an increase in CA concentration. The high-resolution bright field TEM image shown in Figure 4c again confirms the sharp interface between the nanorod core and the shell. The periodicity of the fringes obtained from the HRTEM studies of the core is 0.25 nm, corresponding to the (101) planes of hexagonal ZnO. The nanoparticles of the CdS shell show a fringe spacing of 0.34 nm that is well matched to the reported value for the (002) plane of hexagonal CdS. The energy-dispersive X-ray spectroscopy (EDX) of ZnO/CdS3 core/shell nanorod arrays revealed that most of the Zn and O atoms were found in the core region, and Cd and S atoms were found in the shell region, as shown in Figures S3a and b, respectively, which is as expected.

ZnO/CdS core/shell nanorod arrays were formed by the well-known surface functionalization reaction of carboxylic acids. CA (citric acid) is a powerful ligand, having three carboxylic acid groups and one hydroxyl (−OH) group. At a particular temperature (40 °C), the CA molecules are adsorbed

23657

dx.doi.org/10.1021/jp3083419 | J. Phys. Chem. C 2012, 116, 23653−23662

on the surfaces of ZnO nanorods by carboxyl groups with an outward orientation of the −OH functional groups. The negative charges of the functionalized surfaces of the ZnO nanorods attracts the Cd^{2+} ions from the aqueous solution of $CdCl_2$, and thin $Cd(OH)_2$ layers were formed on the ZnO nanorods. After injection of the sulfur source in the solution, CdS layers were formed on the surfaces of ZnO nanorods by substitution of the OH^- ions by S^{2-} ions. As the concentration of the CA increased, the CdS shell layers became gradually uniform along with an increase in shell thickness. The possible mechanisms[44] of the formation of the ZnO/CdS core/shell nanorod arrays are schematically described in Figure 5.

The optical absorption spectra of the uncoated ZnO nanorods and core/shell nanorod arrays with varying shell thickness are shown in Figure 6. The uncoated ZnO shows an
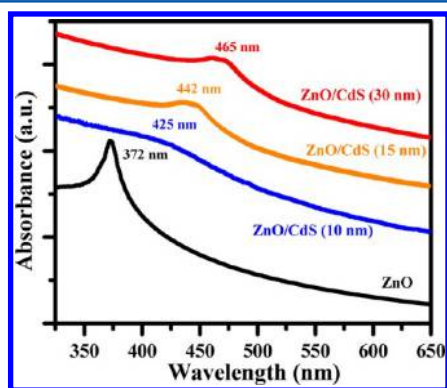

Figure 6. Optical absorbance spectra of the uncoated ZnO nanorods, and ZnO/CdS coreshell nanorod arrays with varying shell thickness.

absorption at 372 nm (3.33 eV). When coated with CdS, the band edge was found to be red-shifted. That is, the absorption spectrum of ZnO/CdS extends to the visible-light region owing to the incorporation of CdS. The absorption in the visible-light region leads to more photogenerated electrons and holes participating in the photocatalytic reaction. Thus, the ZnO/CdS core/shell nanorod arrays exhibits promising application as photocatalysts under visible light compared to pure ZnO. Obviously, ZnO/CdS3 at 465 nm (2.67 eV) possesses a stronger visible light absorption than other samples, which may lead to enhanced visible light degradation efficiency.

Figure 7a shows the PL spectra of the ZnO nanorods and ZnO/CdS core/shell nanorod arrays recorded using an excitation at 325 nm. CdS nanoparticles were excited at 400 nm. The first principles full potential electronic band structure

calculations of $ZnO^{38,39}$ suggest that indirect or direct band gap mainly depends on the crystal structure.[40,41] ZnO possesses a highly ionic lattice, the valence band is composed of oxygen 2p orbitals strongly hybridized with Zn 3d states, and the conduction band consists mostly of excited states of Zn^{2+}. In ZnO nanostructures, different trap levels were observed at energies from 0 to 1 eV below the conduction band (CB) edge at temperatures from −200 to 40 °C.[42] In our studies (Figure 7a, PL of ZnO, curve a), the strong UV emission at 380 nm (3.26 eV) originated from the excitonic recombination corresponding to the band edge emission of ZnO. A broad peak is observed at lower energy 498 nm (2.49 eV). This peak probably comes from the following defects:[30] (1) transition from CB to deep acceptor levels (O_i or O_{Zn}); (2) transition from deep donor levels ($V_O Zn_i$) to VB; (3) transition from shallow donor levels (Zn_i) to shallow acceptor levels (V_{Zn} and O_i), where

$$V_{Zn} = \text{vacant Zn}$$

$$V_O = \text{vacant O}$$

$$Zn_i = \text{interstitial Zn}$$

$$O_i = \text{interstitial O}$$

$$V_O Zn_i = \text{complex of } V_O \text{ and } Zn_i$$

$$O_{Zn} = \text{substitution of O at Zn position}$$

The band gap (E_g) of ZnO nanorods is 3.26 eV and some shallow and deep trap levels lie between 0.77 eV below the CB. Pure hexagonal CdS nanoparticles exhibit an emission peak around 504 nm (2.46 eV). The growth of the CdS shell on the ZnO core causes almost immediate quenching of the emission of ZnO and a new emission peak around 460 nm appears. This new peak experiences a red shift with increasing shell thickness of CdS. The maximum red shift of 110 nm (compared with ZnO) was observed for the core/shell nanorod array ZnO/CdS, which has a shell thickness of 30 nm. The conduction band offset between bulk CdS and ZnO is 0.20 eV, as shown in Figure 10. The band gap of CdS depends on the shell thickness through quantum confinement effect. With increase in shell thickness, the band gap of CdS decreases and consequently lowers the conduction band offset value. The smaller conduction band offset between CdS and ZnO (Figure 10) is responsible for the red shift of absorption and emission bands.

It should be noted that when the CdS precursors were not added to the solution of the core NRs in a dropwise manner,
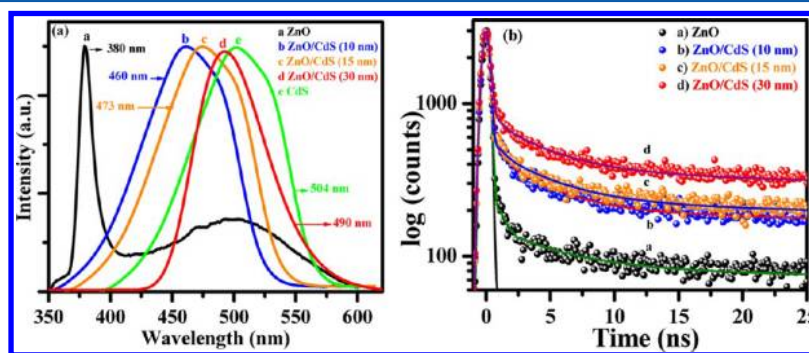

Figure 7. (a) Photoluminescence spectra and (b) photoluminescence decay curves of the uncoated ZnO nanorods, and ZnO/CdS core/shell nanorods with different shell thickness.

the rate of growth of the shell increased. The PL band of resulting core/shell structures shifted to 504 nm, corresponding to the spectral position of pure CdS. This stage indicates the completion of the ion-exchange reaction between $[Zn^{2+}O^{2-}]$ ions and $[Cd^{2+}S^{2-}]$ ions under this fast growth condition, and the consumption of the core resulted in pure CdS NRs.[43]

Figure 7b shows the PL decay curves of the uncoated ZnO nanorods and ZnO/CdS core/shell nanorod arrays with varying shell thickness. The experimental curves have been fitted with three ($n = 3$) exponential decay response function as given by eq 5.[32]

$$P(t) = b + \sum_{i}^{n} \alpha_i \exp\left(-\frac{t}{\tau_i}\right)$$

(5)

here, n is the number of discrete emissive species, b is a baseline correction ("dc" offset), and α_i and τ_i are pre-exponential factors and excited-state fluorescence lifetimes associated with the ith component, respectively.

The values of goodness of fit parameter, χ^2, near unity, as shown in Table 3, indicate a good fit to experimental data. The

Table 3. Absorbance Band, PL Band, Current, and Photocatalytic Efficiency of ZnO and ZnO/CdS Core/Shell Nanorod Arrays with Varying Shell Thickness

sample	shell thickness (nm)	absorbance band (nm)	PL band (nm)	current (A)	photocatalytic efficiency (%)
ZnO		372	380	9.22×10^{-7}	70.0
ZnO/CdS1	10	425	460	8.09×10^{-6}	85.0
ZnO/CdS2	15	442	473	1.62×10^{-5}	91.5
ZnO/CdS3	30	465	490	1.75×10^{-5}	98.0

average decay time $\langle \tau \rangle$ calculated using eq 6[32] increases continuously with the increase in shell thickness.

$$\left\langle \tau \right\rangle = \sum_{i=1}^{n} f_i \tau_i$$

(6)

where the fractional contribution f_i of each decay component was estimated by the relation[32]

$$f_i = \alpha_i / \sum \alpha_i$$

(7)

The slow component (τ_1) may be due to the near band edge relaxation of ZnO. The trap level established at 0.77 eV below CB rapidly traps a photogenerated CB electron (e^-_{CB}). This electron subsequently interacts with a valence band (VB) hole (h^+_{VB}) either radiatively or nonradiatively. As the trapping time for the electron is faster than that for the hole, the faster component (τ_2) in the observed decay kinetics of uncoated ZnO can be assigned to recombination of trapped electrons and holes in the VB. As the time progresses, the electrons from the lower states of the CB move to the shallow trap and then to the deeper trap. Hence, the slower component (τ_3) can be assigned to the recombination of the trapped electrons and trapped holes of different trap depth. The core/shell nanorod arrays give longer decay times than does the uncoated ZnO because of the spatial separation of the charges in the type-II core/shell nanorod arrays, that is, the electrons in the ZnO core and holes in the CdS shell. This reduces the oscillator strength due to the

smaller overlap between electron and hole wave functions and consequently enhances the lifetime.[48] This long-lived charge-separated states make the core/shell nanorods most suitable for photocatalytic and photovoltaic solar cell applications.

Figure 8 shows the current−voltage (I−V) curves for uncoated ZnO nanorods, CdS nanoparticles, and ZnO/CdS
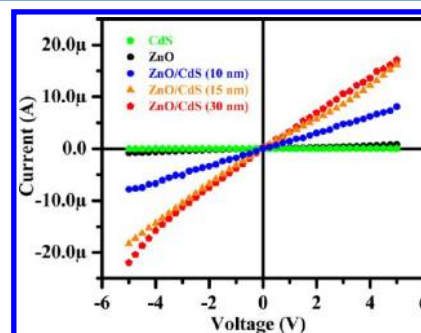

Figure 8. I−V curves of uncoated ZnO nanorods, CdS nanoparticles, and ZnO/CdS core/shell nanorods with different shell thicknesses.

core/shell nanorod arrays with varying shell thickness. The linear I−V curves in ZnO nanorods, CdS nanoparticles, and ZnO/CdS core/shell nanorod arrays with varying shell thickness suggest that ohmic contacts[44] were established between the electrodes and the materials. A 16-fold increase in current is observed with core/shell ZnO/CdS nanorods having shell thickness of 30 nm (ZnO/CdS3), comparing with bare ZnO nanorods and CdS nanoparticles. Moreover, the type-II alignment between ZnO and CdS is also a significant factor toward the enhanced electrical properties. In fact, the energy difference between the conduction band edges of the CdS sensitizer and ZnO is the driving force for the injection of generated electrons from CdS into ZnO. Hence, the 30 nm CdS shell/ZnO nanorod arrays seems to be the best candidate for a photocatalyst and photovoltaic solar cell. Qualitatively, the main reason is that the increased shell thickness is suitable for the generated electrons and holes to travel a shorter path and thus recombination losses are greatly reduced.

The degradation of RhB was used to assess the solar photocatalytic activity of bare ZnO nanorods, CdS nano-particles, and ZnO/CdS core/shell nanorod arrays with varying shell thickness and the results are shown in Figure 9a. All the samples of ZnO/CdS core/shell nanorod arrays exhibit higher photocatalytic activity than bare ZnO and CdS. The degradation rate is as follows: CdS < ZnO < ZnO/CdS1 < ZnO/CdS2 < ZnO/CdS3. ZnO/CdS3 has the best photo-catalytic performance among all the five samples. The kinetics of degradation of RhB under solar light was also investigated. Figure 9b shows a linear relationship between $\ln(C_0/C)$ and reaction time, indicating that the photodegradation of RhB follows first-order kinetics. The apparent rate constants were determined as 0.011, 0.0035, 0.019, 0.025, and 0.039 min^{-1} for ZnO, CdS, ZnO/CdS1, ZnO/CdS2, and ZnO/CdS3, respectively. The order of rate constants is summarized as follows: ZnO/CdS3 > ZnO/CdS2 > ZnO/CdS1 > ZnO > CdS, which is consistent with the conclusions of photocatalytic degradation curves presented in Figure 9a.

Photocatalytic Mechanism. It has been widely accepted that hydroxyl radicals (OH•) generated by the illumination are the main species responsible for the degradation of pollutant molecules. The formation of OH• on the surface of
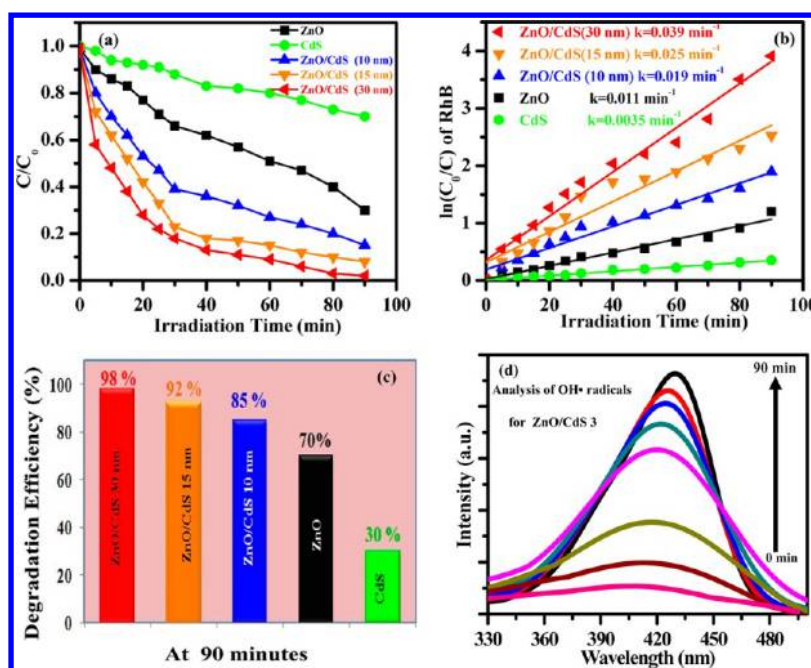
Figure 9. (a) Degradation rate of RhB under simulated solar radiation, (b) the plot of $\ln(C_0/C)$ with irradiation time of solar light, (C_0 is the initial concentration of RhB after absorption; C is the concentration of RhB after photoirradiation) for ZnO, CdS, ZnO/CdS core/shell nanorod arrays having different shell thickness, (c) degradation efficiency of ZnO nanorods, CdS nanoparticles, and ZnO/CdS core/shell nanorod arrays with varying shell thickness on the photodegradation of RhB, and (d) fluorescence spectra measured during illumination of ZnO/CdS3 using terephthalic acid (excitation at 315 nm).

photocatalysts was detected by the PL technique using terephthalic acid (TA) as a probe molecule, which readily reacts with OH$^\bullet$ to produce the highly fluorescent product, 2-hydroxyterephthalic acid (TAOH). The PL intensity of TAOH was proportional to the amount of OH$^\bullet$ produced on the surface of photocatalysts. The maximum emission intensity in PL spectra was recorded at 425 nm by the excitation of 315 nm and the results are shown in Figure 9d. It can be seen that the PL intensity increases gradually with increasing irradiation time, indicating OH$^\bullet$ is formed during this photocatalytic process under natural sunlight. From the linear increase of fluorescence intensity versus time it can be concluded that the formation of OH$^\bullet$ is proportional to the irradiation time.

The enhancement of the photocatalytic efficiency of ZnO/CdS3 could be ascribed to favorable synergistic effect between CdS and ZnO. The band alignment between the core of ZnO and the shell of CdS is shown (Figure 10) in the schematic diagram. The position of CdS and ZnO bands has a type-II alignment where the conduction band edge of ZnO is located between the conduction band and the valence band of CdS. In this configuration, when the electron−hole pairs are generated by visible-light excitation in CdS nanoparticles (shell) the photoelectrons can be transferred to the conduction band of ZnO, which facilitates the charge separation process of the electron−hole pairs before they recombine. When the ZnO/CdS3 photocatalyst is irradiated by solar light, electron−hole pairs are generated in CdS. The electrons from the conduction band of CdS are quickly transferred to the conduction band of ZnO, leading to a high concentration of the electrons in the CB of ZnO. The time required for the transfer of the electron is about 18 ps, which is smaller than the electron's lifetime in CdS.[46] Once the electrons diffuse into the CB of ZnO, the probability of its decay is small because there can be no free hole in ZnO under visible excitation. As a result, electrons
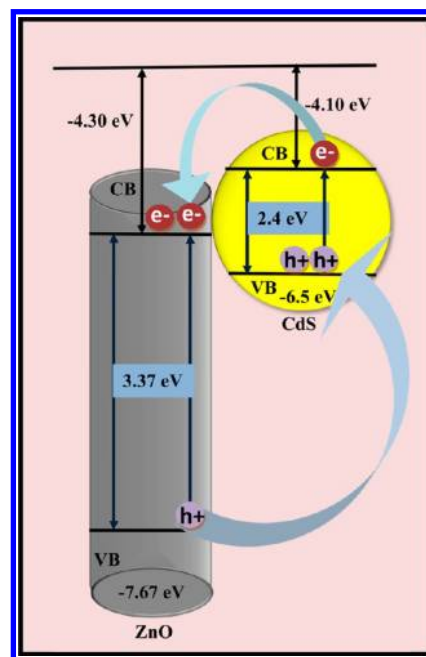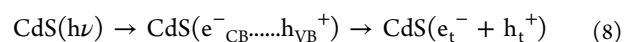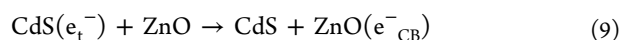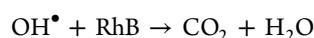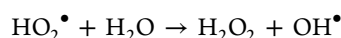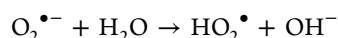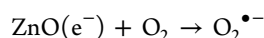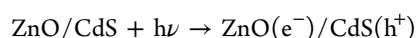

Figure 10. Schematic diagram of the ZnO/CdS core/shell nanorod arrays, showing the type-II band gap alignment: electron−hole pair generation by incident photons and electron injection from the excited CdS shell into the ZnO core.

accumulate in the CB of ZnO and the holes accumulate in the valence band of CdS. In this way, charge separation is achieved. The above charge transfer process can be summarized in the following manner:[46]

$$CdS(h\nu) \rightarrow CdS(e^-_{CB}......h_{VB}^+) \rightarrow CdS(e_t^- + h_t^+) \quad (8)$$

$$CdS(e_t^-) + ZnO \rightarrow CdS + ZnO(e^-_{CB}) \qquad (9)$$

where e^-_{CB} and h_{VB}^+ stand for the electron in the conduction band and hole in the valence band, respectively. Again, e_t^- and h_t^+ are the electrons and the holes, respectively, trapped on the surface of the nanoparticles. Meanwhile, the holes generated on CdS VB are not transferred to the corresponding band of ZnO due to the CdS VB being more cathodic than that of ZnO. Consequently, a high concentration of holes is achieved in the VB of the CdS nanoparticles. Holes in CdS could potentially react with water adhering to the surface of the CdS nanoparticles to form highly reactive hydroxyl radicals (OH$^\bullet$). It is possible that the holes themselves directly oxidize the organic molecules. Subsequently, the CB electrons (e$^-$) accumulated on the surface of ZnO are scavenged by dissolved oxygen molecules in water to yield highly oxidative species such as superoxide radical anion $O_2^{\bullet-}$, producing hydroxyl radical OH$^\bullet$, which is a strong oxidizing agent to decompose the organic dye. The proposed mechanism for the photocatalytic decomposition of organic dye by ZnO/CdS core/shell nanorod arrays can be described as follows:[49]

$$ZnO/CdS + h\nu \rightarrow ZnO(e^-)/CdS(h^+)$$

$$ZnO(e^-) + O_2 \rightarrow O_2^{\bullet-}$$

$$O_2^{\bullet-} + H_2O \rightarrow HO_2^{\bullet} + OH^-$$

$$HO_2^{\bullet} + H_2O \rightarrow H_2O_2 + OH^{\bullet}$$

$$H_2O_2 \rightarrow 2OH^{\bullet}$$

$$OH^{\bullet} + RhB \rightarrow CO_2 + H_2O$$
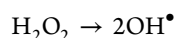
Generally, the improved photocatalytic efficiency of ZnO/CdS compared to pure ZnO and CdS (Figure 9c) results from the efficient charge separation and the efficient interfacial charge transfer. In addition, the photocatalytic efficiencies are also related to the loading amount of citric acid. With increase in the shell thickness (10, 15, and 30 nm), the photocatalytic efficiency of the core/shell nanostructure increases. When ZnO/CdS3 was added to the RhB aqueous solution, the solution decolorized gradually with the increase in irradiation time (90 min). It is confirmed by our experiments that the core/shell nanorod arrays having a shell thickness of 30 nm displays the highest photocatalytic activity for degradation of RhB by solar light, which might come from the well dispersion and relative suitable coverage of CdS nanoparticles on ZnO nanorods. Thus, ZnO nanorods sensitized by CdS shell can be used to fabricate highly efficient photocatalysts for the degradation of organic pollutants under sunlight and can also be used as solar energy conversion materials.

CONCLUSIONS

ZnO/CdS type-II core/shell nanorod arrays were prepared by a surface-functionalized method. Citric acid was used to maintain the uniform growth of core/shell nanorod arrays and also to control the shell thickness. Core/shell nanorods provide a unique system for the study of strain in shell growth. All of the diffraction peaks shift to lower d-spacings (higher 2θ) as a function of shell thickness. The coupling of the two semiconductors enhanced the visible light absorbing capability of these core/shell nanorod arrays. These nanorod arrays exhibit longer lifetime, higher photocatalytic activity, and enhancement in current than pure ZnO and CdS. The

formation of hydroxyl radicals (OH$^\bullet$) on the surface of visible-light illuminated nanorod arrays was detected by the photoluminescence technique using terephthalic acid as probe molecule. Finally, a mechanism has been proposed based on band alignment to elucidate the enhancement of efficiency of ZnO/CdS photocatalysts. Our findings thus prove that type-II core/shell ZnO/CdS nanorod arrays can serve as highly efficient candidates for photocatalytic and photovoltaic applications.

ASSOCIATED CONTENT

Ⓢ Supporting Information

Table S1: Different loading of citric acid (CA) for synthesizing ZnO/CdS core/shell nanorod arrays with varying shell thickness. Figure S1: Williamson−Hall plot of $\beta \cos \theta/\lambda$ against $\sin \theta/\lambda$ for (a) ZnO/CdS1 and (b) ZnO/CdS2. Figure S2: TEM images of (a) ZnO/CdS1 and (b) ZnO/CdS2. Figure S3: EDX analysis of the marked region in Figure 4b corresponding to (a) core and (b) shell. This material is available free of charge via the Internet at http://pubs.acs.org.

AUTHOR INFORMATION

Corresponding Author

*E-mail: ashok@chemistry.iitd.ernet.in. Tel.: 91-11-26591511. Fax: 91-11-26854715.

Notes

The authors declare no competing financial interest.

ACKNOWLEDGMENTS

REFERENCES

(1) Hoffmann, M. R.; Martin, S. T.; Choi, W.; Bahnmann, D. W. *Chem. Rev.* **1995**, *95*, 69−96.
(2) O'Regan, B.; Grätzel, M. *Nature* **1991**, *353*, 737−740.
(3) Barbé, C. J.; Arendse, F.; Comte, P.; Jirousek, M.; Lenzmann, F.; Shklover, V.; Grutzel, M. *J. Am. Ceram. Soc.* **1997**, *80*, 3157−31571.
(4) Asbury, J. B.; Wang, Y. Q.; Lian, T. Q. *J. Phys. Chem. B* **1999**, *103*, 6643−6647.
(5) Grätzel, M. *Nature* **2001**, *414*, 338−344.
(6) Kaidashev, E. M.; Lorenz, M.; Wenckstern, H. V.; Rahm, A.; Semmelhack, H. C.; Han, K. H.; Benndorf, G.; Bundesmann, C.; Hochmuth, H.; Grundmann, M. *Appl. Phys. Lett.* **2003**, *82*, 3901−3903.
(7) Chou, T. P.; Zhang, Q. F.; Fryxell, G. E.; Cao, G. Z. *Adv. Mater.* **2007**, *19*, 2588−92.
(8) Zhang, Q. F.; Chou, T. P.; Russo, B.; Jenekhe, S. A.; Cao, G. Z. *Angew. Chem., Int. Ed.* **2008**, *47*, 2402−2406.
(9) Law, M.; Greene, L. E.; Johnson, J. C.; Saykally, R.; Yang, P. D. *Nat. Mater.* **2005**, *4*, 455−459.
(10) Bater, J. B.; Aydil, E. S. *Sol. Energy Mater. Sol. Cells* **2006**, *90*, 607−622.
(11) Nayak, J.; Lohani, H.; Bera, T. K. *Curr. Appl Phys.* **2011**, *11*, 93−97.
(12) Gerischer, H.; Luebke, M. J. *Electroanal. Chem.* **1986**, *204*, 225−227.
(13) Robel, I.; Subramanian, V.; Kuno, M.; Kamat, P. V. *J. Am. Chem. Soc.* **2006**, *128*, 2385−2393.
(14) Plass, R.; Serge, P.; Krüger, J.; Grätzel, M. *J. Phys. Chem. B* **2002**, *106*, 7578−7580.

(15) Blackburn, J. L.; Selmarten, D. C.; Ellingson, R. J.; Jones, M.; Micic, O.; Nozik, A. J. *J. Phys. Chem. B* **2005**, *109*, 2625−2631.

(16) Xie, Y.; Heo, S. H.; Kim, Y. N.; Yoo, S. H.; Cho, S. O. *Nanotechnology* **2010**, *21*, 015703−015710.

(17) Vogel, R.; Hoyer, P.; Weller, H. *J. Phys. Chem.* **1994**, *98*, 3183−3188.

(18) Zhou, H.; Qu, Y.; Zeida, T.; Duan, X. *Energy Environ. Sci.* **2012**, *5*, 6732−6743.

(19) Ramanathan, K.; Contreras, M. A.; Perkins, C. L.; Asher, S.; Hasoon, F. S.; Keane, J.; Young, D.; Romero, M.; Metzger, W.; Noufi, R.; et al. *Prog. Photovolt.: Res. Appl.* **2003**, *11*, 225−230.

(20) Guo, M.; Diao, P.; Wang, X. D.; Cai, S. M. *J. Solid State Chem.* **2005**, *178*, 3210−3215.

(21) Hosono, E.; Fujihara, S.; Honma, I.; Zhou, H. S. *Adv. Mater.* **2005**, *17*, 2091−2094.

(22) Zhang, Y.; Xie, T. F.; Jiang, T. F.; Wei, X.; Pang, S.; Wang, X.; Wang, D. *J. Nanotechnology* **2009**, *20*, 155707−155713.

(23) Baxter, J. B.; Aydil, E. S. *Appl. Phys. Lett.* **2005**, *86*, 053114−053116.

(24) Tak, Y.; Hong, S. J.; Lee, J. S.; Yong, K. *J. Mater. Chem.* **2009**, *19*, 5945−5951.

(25) Seol, M.; Kim, H.; Tak, Y.; Yong, K. *Chem. Commun.* **2010**, *46*, 5521−5523.

(26) Joo, J.; Kim, D.; Yun, D. J.; Jun, H.; Rhee, S. W.; Lee, J. S.; Yong, K.; Kim, S.; Jeon, S. *Nanotechnology* **2010**, *21*, 325604−325609.

(27) Salazar, R.; Delamoreanu, A.; Clement, C. L.; Ivanova, V. *Energy Procedia* **2011**, *10*, 122−127.

(28) Tak, Y.; Hong, S. J.; Lee, J. S.; Yong, K. *Cryst. Growth Des.* **2009**, *9*, 2627−2632.

(29) Kundu, P.; Deshpande, P. A.; Madras, G.; Ravishankar, N. *J. Mater. Chem.* **2011**, *21*, 4209−4216.

(30) Lin, C.-C.; Li, Y.-Y. *Mater. Chem. Phys.* **2009**, *113*, 334−337.

(31) Oliveria, J. F. A.; Milao, T. M.; Araujo, V. D.; Moreira, M. L.; Longo, E.; Bernardi, M. I. B. *J. Alloys Compd.* **2011**, *509*, 6880−6883.

(32) Das, K.; De, S. K. *J. Phys. Chem. C* **2009**, *113*, 3494−3501.

(33) Qamar, M.; Kim, S. J.; Ganguli, A. K. *Nanotechnology* **2009**, *20*, 455703−455711.

(34) Wang, Q.; Pan, D.; Jiang, S.; Ji, X.; An, L.; Jiang, B. *J. Lumin.* **2006**, *118*, 91−98.

(35) Hines, M. A.; Guyot-Sionnest, P. *J. Phys. Chem.* **1996**, *100*, 468−471.

(36) Dabbousi, B. O.; Rodrigeuez-Viejo, J.; Mikulec, F. V.; Heine, J. R.; Mattoussi, H.; Ober, R.; Jensen, K. F.; Bawendi, M. G. *J. Phys. Chem. B* **1997**, *101*, 9463−9475.

(37) Peng, X. G.; Schlamp, M. C.; Kadavanich, A. V.; Alivisatos, A. P. *J. Am. Chem. Soc.* **1997**, *119*, 7019−7029.

(38) Ahuja, R.; Fast, L.; Eriksson, O. *J. Appl. Phys.* **1998**, *83*, 8065−8067.

(39) Bera, A.; Basak, D. *Appl. Phys. Lett.* **2009**, *94*, 163119−163121.

(40) Daude, N.; Gout, C.; Jouanin, C. *Phys. Rev. B* **1977**, *15*, 3229−3235.

(41) Asahi, R.; Taga, Y.; Mannstadt, W.; Freeman, A. *J. Phys. Rev. B* **2000**, *61*, 7459−7465.

(42) He, H.; Wang, Y.; Wang, J.; Ye, Z. *Phys. Chem. Chem. Phys.* **2011**, *13*, 14902−14905.

(43) Xu, F.; Vyacheslav, V.; Yimei, Z.; Hanying, B.; Rea, A.; Valappil, N. V.; Su, W.; Gao, X.; Kuskovsky, I. L.; Matsui, H. *J. Phys. Chem. C* **2009**, *113*, 19419−19423.

(44) Datta, A.; Panda, S. K.; Chaudhuri, S. *J. Phys. Chem. C* **2007**, *111*, 17260−17264.

(45) Sungjee, K.; Fisher, B.; Eisler, H.-J.; Bawendi, M. G. *J. Am. Chem. Soc.* **2003**, *125* (38), 11466−11467.

(46) Nayak, J.; Sahu, S. N.; Kasuya, J.; Nozaki, S. *Appl. Surf. Sci.* **2008**, *254*, 7215−7218.

(47) Kar, A.; Datta, A.; Patra, A. *J. Mater. Chem.* **2010**, *20*, 916−922.

(48) Ivanov, S. A.; Piryatinski, A.; Nanda, J.; Tretiak, S.; Zavadil, K. R.; Wallace, W. O.; Werder, D.; Klimov, V. I. *J. Am. Chem. Soc.* **2007**, *129*, 11708−11719.

(49) Xiao, M.; Wang, L.; Wu, Y.; Huang, X.; Dang, Z. *Nanotechnology* **2008**, *19*, 015706−015713.

(50) Ghosh, P.; Kar, A.; Patra, A. *J. Appl. Phys.* **2010**, *108*, 113506−113513.